Journal of Environmental Chemical Engineering 11 (2023) 109366

Contents lists available at ScienceDirect

Journal of Environmental Chemical Engineering

journal homepage: www.elsevier.com/locate/jece

Direct Z-scheme g-C_3N_4/TiO_2 heterojunction porous nanotubes: An ingenious synthesis strategy to enhance photocatalytic activity

Sheng-Zhe Zhao [a], Ran Lu [a], Yi Yang [a], Yun Lu [b,*], Raul D. Rodriguez [c], Jin-Ju Chen [a,*]

[a] School of Materials and Energy, University of Electronic Science and Technology of China, Chengdu 610054, PR China
[b] School of Electronic Science and Engineering, University of Electronic Science and Technology of China, Chengdu 610054, PR China
[c] Tomsk Polytechnic University, 30 Lenin Ave, 634050 Tomsk, Russia

ARTICLE INFO

Keywords:
Electrospinning
Heterostructure
G-C_3N_4/TiO_2
Nanotubes
Photocatalysis

ABSTRACT

Photocatalysis has a broad prospect for generating H_2 and reactive oxygen species. In this study, porous nanotubular g-C_3N_4/TiO_2 photocatalysts were obtained via electrospinning combined with an innovative vapor deposition approach. The waste foam was used as the precursor material for TiO_2 nanotubes, reducing production cost and benefiting resource recovery. The modification of g-C_3N_4 onto TiO_2 nanotubes provided extensive active sites with an increased specific surface area and produced the heterojunction to improve charge separation. The g-C_3N_4/TiO_2 nanotubes displayed remarkable photocatalytic effects in the degradation of organic dye with a removal efficiency of 93.4% and H_2 evolution reaction performing at 4122 $\mu mol \cdot g^{-1} \cdot h^{-1}$ under simulated sunlight. Photocatalytic activation product analyses and density functional theory (DFT) calculations demonstrated a possible photogenerated carriers transfer pathway. This work provides a way to prepare multifunctional porous nanotubes using a facile synthesis method from abandoned resources with implications for environmental remediation and hydrogen generation.

1. Introduction

In recent years, the efficient utilization of solar energy has shown great significance for energy conservation and environmental remediation. [1,2] Photocatalysis has been extensively studied and achieved remarkable results, including hydrogen production by water splitting, reduction of carbon dioxide to alcohols and other valuable chemicals, and pollutant decomposition. [3–5] Among common semiconductor photocatalysts, titanium oxide (TiO_2) shows great value owing to its suitable band gap (~ 3.2 eV), low fabrication cost, good chemical stability, and environmental friendliness. [6–8] Many pieces of research focused on further improving photocatalyst performance. [9,10] On the one hand, photocatalysts with special nanoscale morphology were designed to obtain more active sites, which could enhance photocatalytic efficiency significantly. [11,12] On the other hand, constructing heterojunction photocatalysts based on TiO_2 and narrow band gap semiconductors was also a popular research direction that allowed tuning the band structure to extend the spectral response range to visible light. [13–15] More importantly, constructing heterogeneous structures could significantly reduce the recombination rate of photo-induced carriers. [16–18].

Graphitic carbon nitride (g-C_3N_4) is an excellent metal-free semiconductor photocatalyst. It has attracted extensive interest because of its superb visible light response, desirable band gap (~ 2.7 eV), low cost, and layered structure conducive to electron transport. [19,20] However, the photocatalytic performance of bulk g-C_3N_4 is limited because its morphology is difficult to control, reducing active sites and specific surface area. [21,22] Therefore, using g-C_3N_4 as a functional component combined with other semiconductors to construct heterostructure photocatalysts makes efficiently exploiting the individual advantages of each material possible. [23,24] Ingeniously designed heterostructures keep the g-C_3N_4 in a dispersed state and reduce the recombination rate of photo-induced electron/hole pairs, thus considerably increasing the photocatalytic efficiency.[25,26] Among these photocatalysts, TiO_2 with g-C_3N_4 can form the unique Z-scheme heterojunction to facilitate electron-hole separation. [27] Therefore, several works on g-C_3N_4/TiO_2 heterostructures with special morphology have been reported. [28].

So far, g-C_3N_4/TiO_2 heterojunctions are obtained mainly by calcining a mixture of nitrogen-rich precursor material (for example, melamine, cyanamide, or urea) and nanoscale TiO_2 in the form of nanoparticles, nanosheets, or nanofibers. However, this calcination way usually leads to the aggregation of g-C_3N_4, reducing the density of active

* Corresponding authors.
E-mail addresses: luyun1501@163.com (Y. Lu), jinjuchen@uestc.edu.cn (J.-J. Chen).

https://doi.org/10.1016/j.jece.2023.109366
Received 16 November 2022; Received in revised form 13 January 2023; Accepted 22 January 2023
Available online 23 January 2023

sites available. [29] Meanwhile, the preparation of g-C_3N_4 by calcination from nitrogen-rich precursors usually requires anaerobic conditions with high preparation costs. [30] Although some mild synthetic methods have been proposed, the crystallinity of those samples is lower than that of calcination. The critical question is how to obtain g-C_3N_4/TiO_2 heterojunctions with good dispersion and high crystallinity. We demonstrate that a way combining the sacrificial template method and vapor deposition provides opens a new approach to achieving this goal.

In this work, we synthesized g-C_3N_4/TiO_2 porous nanotubes photocatalysts via sacrificial templates followed by subtle vapor deposition. The TiO_2 nanotubes were obtained with polystyrene nanofibers as sacrificial templates prepared by electrospinning. Then TiO_2 nanotubes were modified by g-C_3N_4 nanosheets to form the g-C_3N_4/TiO_2 heterojunction via sublimating urea in a cleverly designed container. The g-C_3N_4 content in the heterojunction could be controllably adjusted to obtain photocatalysts with significant performance for the photodegradation of methyl orange (MO) and the H_2 evolution under simulated sunlight. This synthesis strategy makes full use of waste resources to reduce the cost, and more importantly, the obtained g-C_3N_4/TiO_2 nanotubes with desirable morphology exhibit outstanding photocatalytic performance.

2. Experimental

2.1. Materials

Experimental materials include waste foam (main components: polystyrene, PS), absolute ethanol (C_2H_6O, 99%), N, N-dimethylformamide (DMF, 99%), urea (CH_4N_2O, 99%), tetrabutyltitanate (TBOT, 99%), 1,4-benzoquinone (BQ, 99%), disodium ethylenediaminetetraacetate (Na_2EDTA, 99%), tert-butyl alcohol (*t*-BuOH, 99%), methyl orange (MO, 96%), and triethanolamine (TEOA, 99%). All chemicals and solvents, purchased from Aladdin, were of analytical grade.

2.2. Fabrication of TiO_2 nanotubes

Clean polystyrene foam (2.5 g) was added to DMF (10 mL) with magnetic stirring at 60 ºC for 1 h to obtain PS/DMF precursor solution. The PS/DMF solution was injected into a syringe that was attached to a high voltage (16 kV). The solution's flow rate was kept at 1 mL/h, and the gap between the positive needle and the negative generator was 20 cm. The humidity during spinning was controlled under 5%. After collection, the white polystyrene nanofibers membrane was successfully obtained and then dried at 85 ºC in vacuum for 12 h to remove residual solvent.

The obtained PS nanofibers were used as sacrificial templates for the preparation of TiO_2 nanotubes, which were first soaked in TBOT/ethanol solution (volume ratio 1:10) to hold 5 min. Then, the resulting PS/TBOT precursor fibres were naturally dried in air after being drained of excess solvent. Finally, the fibres were calcined at 550 ºC for 2 h at a rate of 2 ºC/min to remove PS templates completely and obtain the TiO_2 nanotubes.

2.3. Fabrication of g-C_3N_4/TiO_2 heterostructures as photocatalysts

The g-C_3N_4 nanosheets were assembled on the surface of TiO_2 nanotubes by an improved vapor deposition. Urea was placed in the bottom of a 100 mL crucible, in which a 30 mL crucible containing 20 mg TiO_2 nanotubes was placed. We made sure that the urea was evenly distributed between the two crucibles. The large crucible was covered with a sealed lid and wrapped with tinfoil to insulate the air. Afterward, the sealed crucible system was transferred into a muffle furnace to calcine at 550 ºC for 1 h with a rate of 5 ºC/min. The mass of urea was 4 g, 6 g, and 8 g, and the obtained g-C_3N_4/TiO_2 nanotubes were named as TC1, TC2, and TC3, respectively. For comparison, pure g-C_3N_4 was also prepared by directly heating urea in a sealed crucible.

The detailed characterizations and photocatalytic performance test of the as-prepared photocatalysts can be found in Supporting Information (SI).

3. Results and discussion

The overall synthetic process of g-C_3N_4/TiO_2 nanotubes is shown in Scheme 1. (i) The primary ingredient of the waste foam is polystyrene (PS), which dissolves in the DMF obtained as the precursor solution and further processes into nanofibers by electrospinning. (ii) The PS nanofibers can absorb the TBOT/ethanol as the template and complete decomposition after calcination resulting in hollow TiO_2 nanotubes. (iii) With the temperature increasing, urea sublimates and consumes the oxygen in the system to form a sealed environment, which provides the condition for growing g-C_3N_4 nanosheets on the inner and outer surface of TiO_2 nanotubes. Meanwhile, the increasing pressure promotes microporous formation on the surface of the nanotubes. This process finally ends with the successful generation of porous g-C_3N_4/TiO_2 nanotubes.

3.1. Characterization

The morphologies of the as-prepared photocatalysts were deduced by scanning electron microscopy (SEM). The surface of the polystyrene template nanofibers is relatively rough and presents a uniform diameter of about 900 nm, as shown in Fig. S1A in SI. The nanofibers' morphology does not change after adsorption of TBOT (Fig. S1B in SI). After calcination, the template nanofibers decompose completely and the TiO_2 nanotube structure is obtained, as shown in Fig. 1A and B. Uniform tubes with a diameter of about 800 nm are observed, and there are many micropores on the nanotubes' surface to increase the specific surface area further. The porous structure formation could be due to the roughness of the template nanofibers. When the humidity is set at 20% during electrospinning, the surface of the obtained template nanofibers is smooth (Fig. S1C in SI). The change in surface roughness may be caused by the different solvent volatilization rates at different humidity. The TiO_2 nanotubes prepared using the smooth template nanofibers show a compact surface in Fig. S1D.

SEM images of g-C_3N_4/TiO_2 heterostructures are shown in Fig. 1C-H. Compared with the pure TiO_2 nanotubes (Fig. 1A and B), although g-C_3N_4/TiO_2 samples still retain the nanotube structure with the same diameter, the surface roughness increases with g-C_3N_4 depositing on the surface of TiO_2 nanotubes. The reason for the formation of porous g-C_3N_4/TiO_2 nanotubes could be explained by the following process. The gaseous urea molecules diffuse into the 3D structure of TiO_2 nanotubes and are adsorbed on the surface of TiO_2, which eventually grows into dispersive g-C_3N_4. The increased pressure from the sublimation of urea molecules and the internal stress in the g-C_3N_4 growth process lead to the increase in the pore size of TiO_2 nanotubes. Therefore, the morphology of g-C_3N_4/TiO_2 nanotubes can be controlled only by changing the amount of urea in the reactant. The TC2 (Fig. 1E and F) shows the best uniformity with enhanced roughness and pore size, while the porous feature of the TC3 (Fig. 1G and H) disappears due to the excessive generation of g-C_3N_4.

The scanning transmission electron microscopy (STEM) image of the TC2 in Fig. 2A clearly shows the porous nanotube structure, and the Fast Fourier Transform (FFT) image in the inset of Fig. 2A shows the heterostructure with good crystallinity. The transmission electron microscopy (TEM) was utilized to analyze the morphology and microstructure further. As shown in Figs. 2B and 2C, TEM images of TC2 show that the g-C_3N_4 nanosheets are uniformly dispersed on the surface of TiO_2 porous nanotubes. The HRTEM image in Fig. 2D demonstrates the lattice spacing of 0.189 nm and 0.324 nm agreeing with the (200) plane of anatase TiO_2 and (002) plane of g-C_3N_4 phase, respectively, revealing the intimate interface between TiO_2 and g-C_3N_4 to form the heterojunction. Therefore, the charge transfer between the TiO_2 and g-C_3N_4

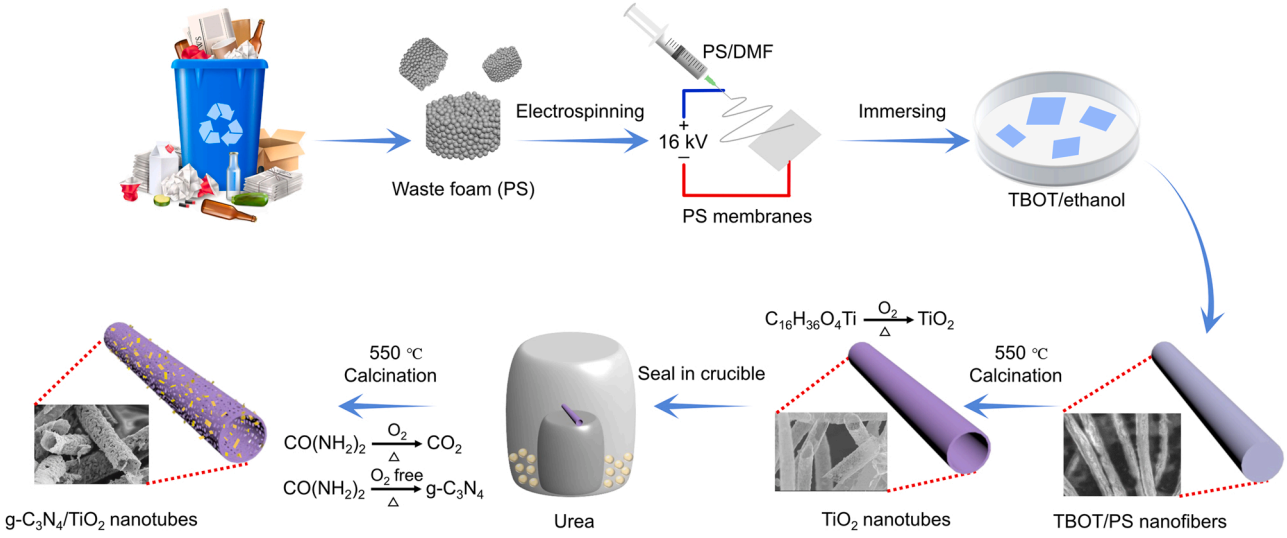

Scheme 1. An illustration for the preparation of porous g-C_3N_4/TiO_2 nanotubes.

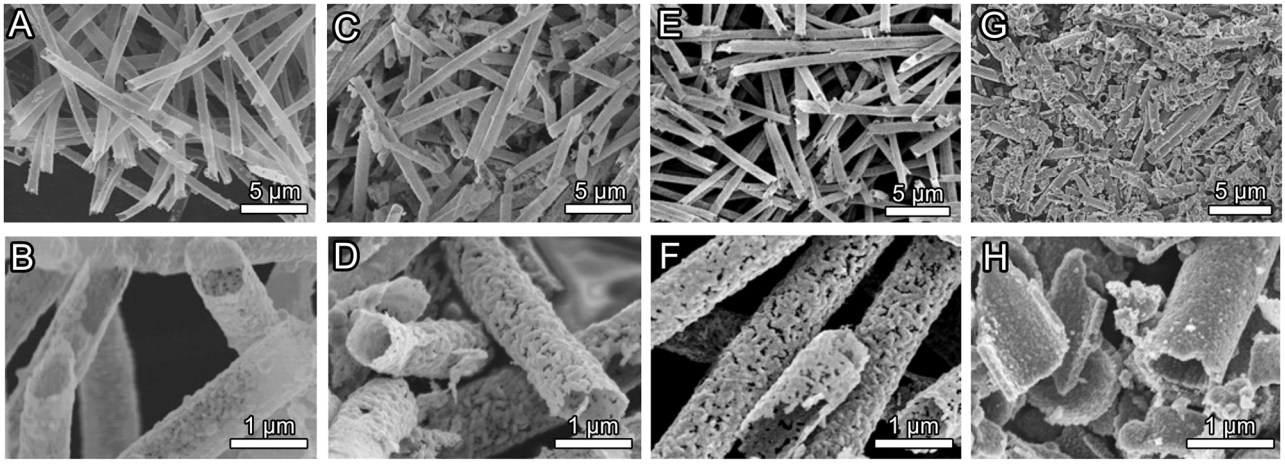

Fig. 1. The SEM images of porous TiO_2 nanotubes (A and B), TC1 (C and D), TC2 (E and F), and TC3 (G and H).

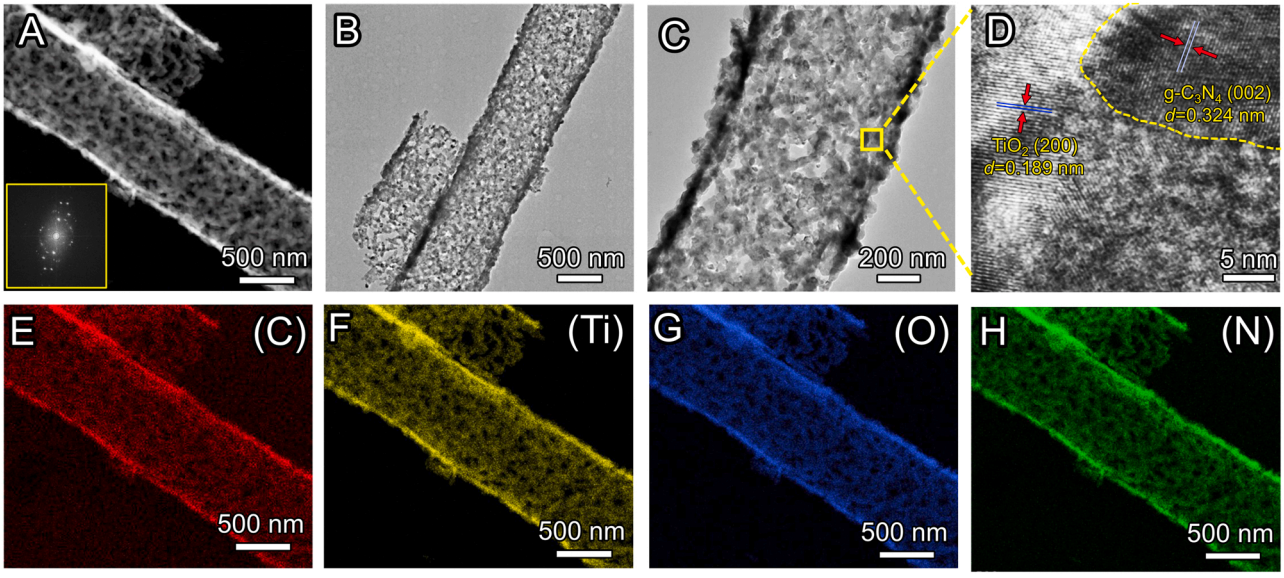

Fig. 2. STEM image (A) and FFT analysis (inset), TEM (B-C), HRTEM (D), and EDS mapping (E-F) of porous g-C_3N_4/TiO_2 (TC2) nanotubes.

will be spatially smooth, which improves photocatalytic efficiency.

Meanwhile, the energy dispersive X-ray spectroscopy (EDS) element mapping of the TC2 nanotubes were recorded to analyze the elemental composition distribution. As shown in Fig. 2E-F, besides Ti and O elements of TiO_2, C and N elements are also detected and homogeneously distributed on the surface of the nanotubes. The N element only comes from g-C_3N_4, which suggests that g-C_3N_4 nanosheets are formed on the surface of TiO_2 nanotubes to construct the g-C_3N_4/TiO_2 heterostructure. EDS spectrum shown in Fig. S2 in SI shows the elemental content of the TC2 sample. The C and N peaks directly prove the existence of g-C_3N_4.

The phase structures of the as-prepared samples were determined by the X-ray diffraction (XRD) as shown in Fig. 3A. It can be clearly observed that the main diffraction peaks of TiO_2 located at 25.45°, 37.95°, 48.20°, 55.16°, and 62.81° correspond to the (101), (004), (200), (211), and (204) planes of anatase TiO_2 (JCPDS 21–1272). [3] For the g-C_3N_4/TiO_2 nanotubes, the peak at 27.4° is assigned to the (002) lattice planes of g-C_3N_4, [13] confirming the formation of g-C_3N_4 on the surface of TiO_2. Meanwhile, the intensity of the (002) diffraction peak gradually increases with urea addition, which shows that the components of g-C_3N_4/TiO_2 heterostructures could be easily controlled by sublimating different amounts of urea.

Fourier transformed infrared (FT-IR) spectra were used to analyze the surface composition of samples. As shown in Fig. 3B, the peak at 680 cm^{-1} for both samples correspond to the vibration of Ti-O-Ti bonds in TiO_2, while peaks at 1241, 1320, 1410, 1564, and 1640 cm^{-1} can be observed for g-C_3N_4/TiO_2 heterostructure, attributed to the aromatic C-N bonds of g-C_3N_4 nanosheets. [29] All the feature peaks originating from g-C_3N_4 and TiO_2 components coexist in the photocatalyst, further demonstrating that the g-C_3N_4 is successfully formed on the TiO_2 nanotubes. To determine the mass fraction of g-C_3N_4 modified on TiO_2 nanotubes, the thermal gravimetric analysis (TGA) was performed from 25 °C to 700 °C at a heating rate of 5 °C/min. As shown in Fig. 3C, all samples showed significant weight loss at 500–580 °C, ascribed to g-C_3N_4 decomposition. The mass percentages of g-C_3N_4 in TC1, TC2, and TC3 heterostructures are 14.6%, 21.3%, and 33.1%, respectively.

The specific surface area and pore volume of as-prepared nanotubes were determined by the nitrogen adsorption/desorption isotherms through the Brunauer-Emmett-Teller (BET) method. Fig. 3D shows that the specific surface area and pore volume of the TiO_2 nanotubes are 14.3 m^2/g and 0.06 cm^3/g, respectively, and the g-C_3N_4/TiO_2 (TC2) possesses a specific surface area of 27.7 m^2/g and pore volume of 0.15 cm^3/g. After the removal of g-C_3N_4 from g-C_3N_4/TiO_2 nanotubes through calcination, the specific surface area of the obtained TiO_2 nanotubes (defined as TiO_2-2, as shown in Fig. S3 in SI) declines to 22.3 m^2/g with a pore volume of 0.11 cm^3/g. Meanwhile, the specific surface area of the pure g-C_3N_4 (Fig. S4 in SI) is 8.9 m^2/g with a pore volume of 0.07 cm^3/g. The results indicate that the innovative vapor deposition approach can effectively increase the surface pores of the TiO_2 nanotubes and restrain the agglomeration of g-C_3N_4, which is consistent with SEM images.

X-ray photoelectron spectroscopy (XPS) was carried out to analyze the surface chemical states of as-prepared samples. The XPS spectra of g-C_3N_4/TiO_2 (TC2) nanotubes in Fig. S5 show the Ti, O, C, and N peaks. High-resolution XPS spectra of Ti 2p in Fig. 4A show peaks at 458.4 eV and 464.2 eV corresponding to Ti $2p_{3/2}$ and Ti $2p_{1/2}$ of TiO_2 in TC2. The distance between the two peaks is about 5.7 eV, proving that the Ti

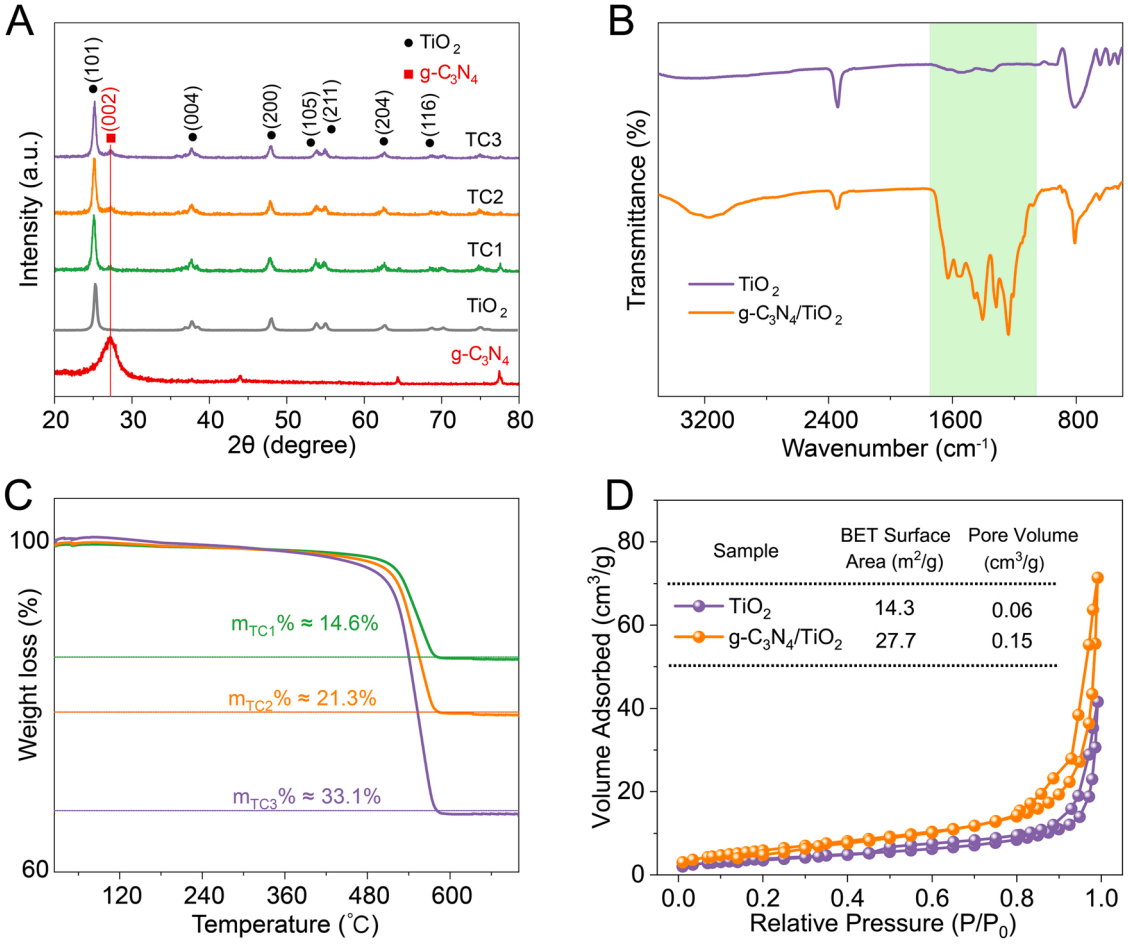

Fig. 3. The XRD patterns of the prepared TiO_2, g-C_3N_4, and g-C_3N_4/TiO_2 samples (A). The FTIR spectra of TiO_2 and g-C_3N_4/TiO_2 (TC2) nanotubes (B). The TGA curves of g-C_3N_4/TiO_2 samples (C). The nitrogen adsorption/desorption isotherms of porous TiO_2 and g-C_3N_4/TiO_2 (TC2) nanotubes (D).

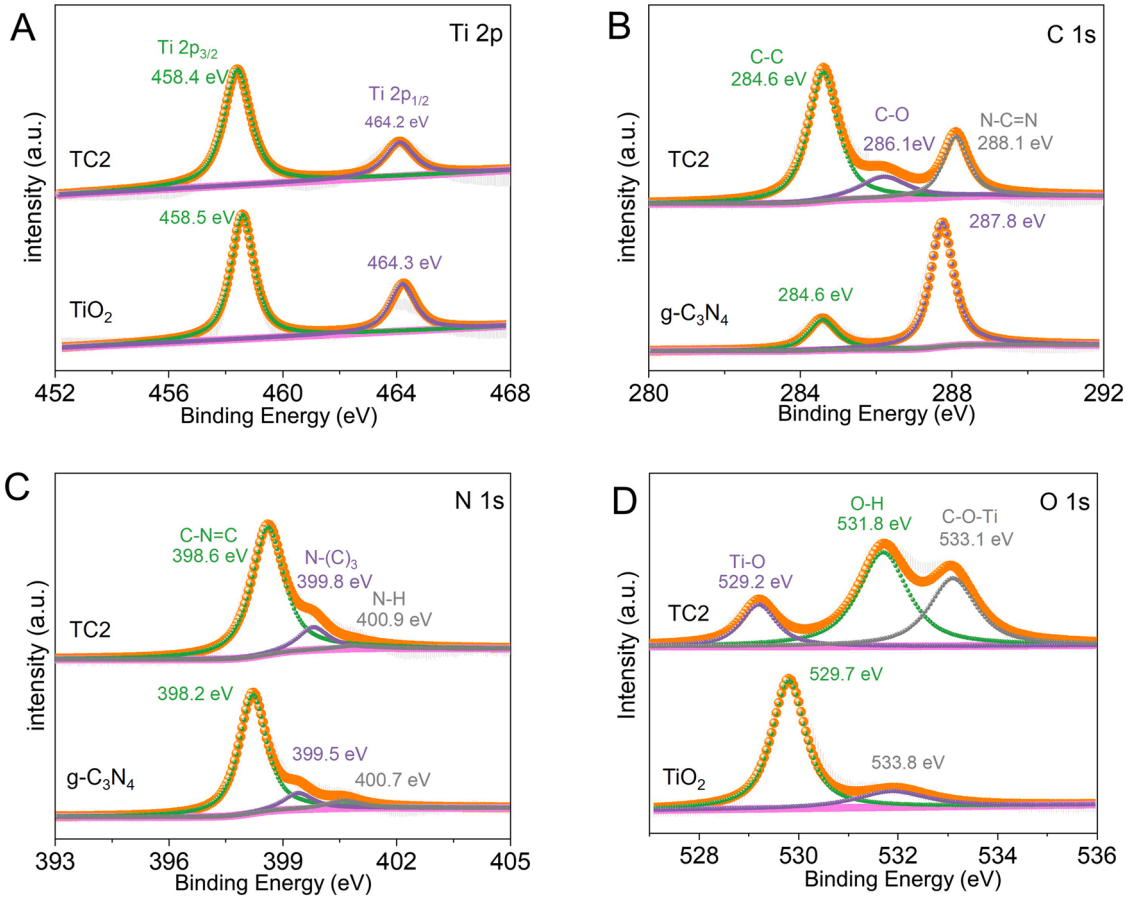

Fig. 4. The high-resolution XPS patterns of Ti 2p (A), C 1 s (B), N 1 s (C), and O 1 s (D) in TiO_2 nanotubes, bulk g-C_3N_4, and g-C_3N_4/TiO_2 (TC2) nanotubes.

element exists in the Ti^{4+} state. [28] The characteristic peaks at 284.6 eV, 286.1 eV, and 288.1 eV in the high-resolution spectrum of C 1 s in TC2 (Fig. 4B) are assigned to the C-C, C-O, and N-C═N groups. In the N 1 s spectrum (Fig. 4C), three peaks in TC2 are deconvolved at 398.6 eV, 399.8 eV, and 400.9 eV corresponding to the groups C═N-C, N-$(C)_3$, and N-H, respectively. It is noted that these three peaks in TC2 shift to higher binding energy compared with those of pure g-C_3N_4, meaning that the g-C_3N_4 on the surface partly lost electrons. [31] The high-resolution O 1 s spectrum (Fig. 4D) for the pure TiO_2 nanotubes is composed of two peaks at 529.7 eV and 533.8 eV, corresponding to the Ti-O bond and surface adsorbed oxygen. For the TC2 nanotubes (Fig. 4D), a new peak appears at 533.1 eV, besides the peaks from the Ti-O band and surface adsorbed oxygen. The peak can be assigned to the C-O-Ti bond, which may form during the urea sublimation reaction. [28] Meanwhile, the Ti-O bond shifts to lower binding energy, meaning that the TiO_2 in g-C_3N_4/TiO_2 gains electrons. [31] These results indicate the electrons move from g-C_3N_4 nanosheets to TiO_2 nanotubes after coupling to achieve Fermi level equilibrium, which effectively confirms the heterostructure between g-C_3N_4 and TiO_2.

The ultraviolet-visible diffuse reflectance spectra (UV-Vis DRS) were used to investigate the optical properties of the photocatalysts. The absorption spectra of the as-prepared samples in the region from 250 to 800 nm are shown in Fig. 5A. The absorption of pure TiO_2 nanotubes is mainly in the UV light region, and the g-C_3N_4 can absorb UV light and an amount of visible light. Compared with pure TiO_2 nanotubes, all g-C_3N_4/TiO_2 composite nanotubes have a significant absorption in the visible spectral range. Meanwhile, the visible light absorption of g-C_3N_4/TiO_2 nanotubes shows a rising trend with the increase of g-C_3N_4 loading, which is attributed to the excellent visible-light photo-response of g-C_3N_4 nanosheets and the remarkable photosensitive effect produced by the heterostructure between TiO_2 and g-C_3N_4. [32,33] Notably, the significant absorption enhance of TC2 and TC3 in the visible light range may be due to the light scattering, which caused by the pores and cracks on the nanotubes formed under heat treatment.

The band gap energies (E_g) of photocatalysts were calculated by the Kubelka-Munk equation: [34].

$$(ah\nu)^n = A(h\nu - E_g)\cdot$$

Where a, $h\nu$, A and E_g represent the absorption coefficient, photon energy, a constant and band gap energy, respectively. [35] The values of n for anatase TiO_2 or TiO_2 based photocatalyst and g-C_3N_4 are correspond to 1/2 and 2. As shown in Figs. 5B and 5C, the band gap energies of pure TiO_2 nanotubes, TC1, TC2, TC3 and g-C_3N_4 can be calculated to be 3.06 eV, 2.87 eV, 2.38 eV, 2.23 eV and 2.86 eV, respectively. It is clear that compared to pure TiO_2 nanotubes, the band gap energies of g-C_3N_4/TiO_2 (TC1, TC2, and TC3) nanotubes are reduced significantly. This phenomenon may be caused by the morphology of nanotubes is favorable for multiple light absorption, and the surface defects (such as porous structure, lattice disorder, oxygen vacancies, etc.), which extend the light absorption range of g-C_3N_4/TiO_2 nanotubes to the visible light region.

The electronic properties and crystal structure of the g-C_3N_4/TiO_2 heterostructure were calculated by using Vienna ab-initio simulation package (VASP). To obtain the lowest energy structure, the g-C_3N_4/TiO_2 composite nanotube structure was fabricated from a unit cell of g-C_3N_4 and a supercell of TiO_2, and the resulting lattice mismatch rate is only 1.07%. [36,37] The band gap is calculated to be 2.81 eV as shown in Fig. 5D, which is close to the experimental value (2.23–2.87 eV). The difference between the theoretical and actual values can be attributed to the percentage of g-C_3N_4 loading and the enhancement of visible light

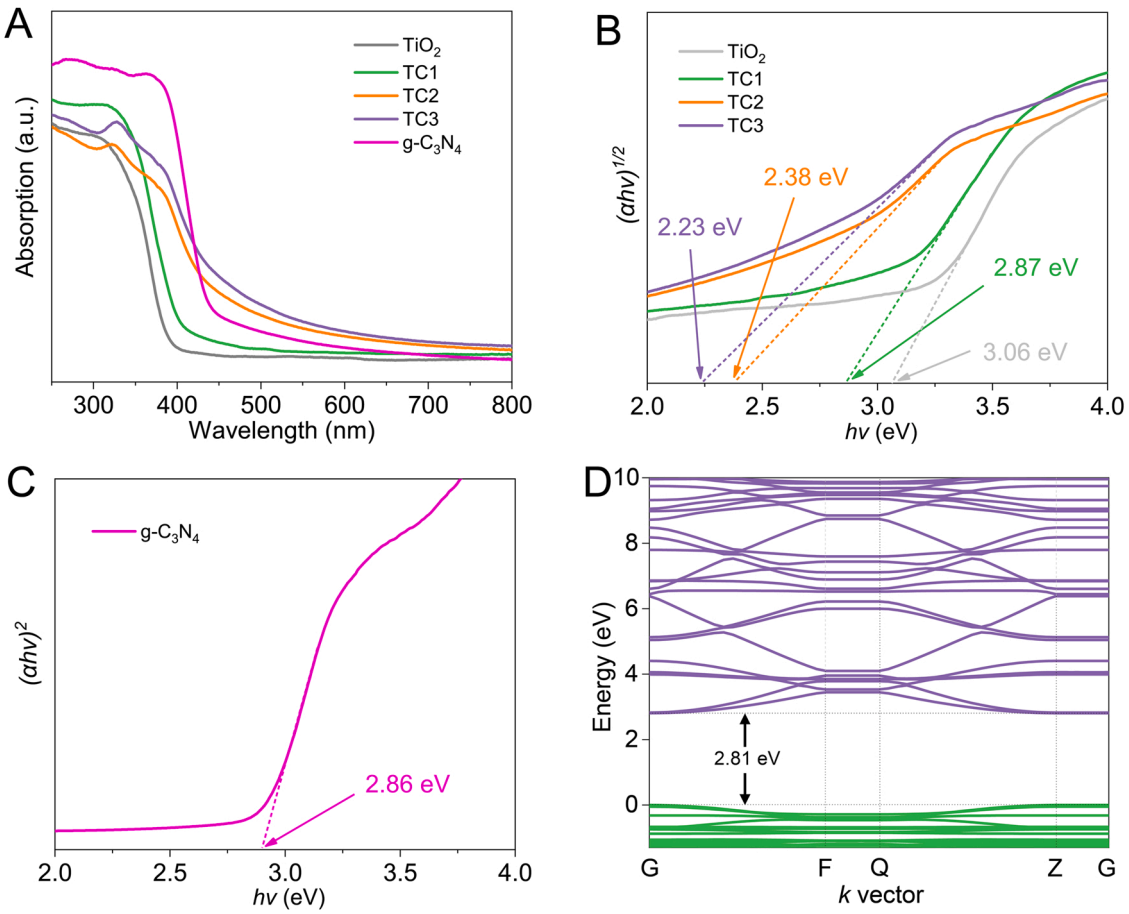

Fig. 5. The DRS spectra of the as-prepared samples (A). The corresponding deduced band gap energy of TiO_2, TC1, TC2, TC3 nanotubes (B), and bulk g-C_3N_4 (C). The electronic band structure of the g-C_3N_4/TiO_2 calculated by VASP (D).

absorption caused by surface defects in actual samples.

3.2. *Photocatalytic performance of g-C_3N_4/TiO_2 porous nanotubes*

To identify the photocatalytic performance, the as-prepared samples were evaluated by the photodegradation of MO under xenon lamp irradiation. The photodegradation rate of MO was investigated by C_t/C_0 (C_0 is the initial MO concentration, and C_t is the concentration of MO at time *t*, which were determined by Lambert-Beer law from the results of UV-Vis spectroscopy). Fig. 6A shows the concentration change of MO during the photodegradation process. After reaching the adsorption/desorption equilibrium in dark (2 h), the photodegradation system showed a certain adsorption effect especial for the TC2, which may be caused by the porous structure of the sample itself and consistent with the BET analysis. After being irradiated by a xenon lamp for 50 min, the TC2 nanotubes exhibit a removal efficiency of 93.4%. This performance is superior to that of TC3 (83.1%) and much higher than TC1 (77.5%) and TiO_2 nanotubes (61.2%). The photodegradation of MO without catalysts is almost negligible. Meanwhile, in order to compare the photocatalytic activities of the samples, their photodegradation rate could be fitted by the pseudo-first-order kinetic analysis $\ln(C_0/C_t)=kt$, where k is the rate constant (min^{-1}). As shown in Fig. 6B, the TC2 presents the highest photodegradation rate and 2.73 times higher than TiO_2 nanotubes, which suggests that the heterostructure could highly improves photocatalytic activity. Fig. S6 (shown in SI) presents the results of MO degradation under visible light irradiation ($\lambda > 420$ nm). It evidences a similar trend to that under full spectrum illumination, with TC2 exhibiting the highest degradation efficiency due to the introduction of g-C_3N_4 to TiO_2 nanotubes, effectively improving the photocatalytic properties. The high specific surface area and enhanced charge carrier separation efficiency are conducive to the high photocatalytic activities of TC2.

The photocatalytic stability of g-C_3N_4/TiO_2 (TC2) composite nanotubes was investigated for the degradation of MO under xenon lamp irradiation. The photocatalyst was washed with ethanol and centrifuged three times for the next test. The results in Fig. 6C show that the catalyst exhibits excellent stability even after four reuse cycles. The photocatalytic efficiency of the g-C_3N_4/TiO_2 (TC2) nanotubes are compared with other photocatalysts in Table S1 (shown in SI). The results shown that the g-C_3N_4/TiO_2 nanotubes with excellent potential in photodegradation of organic pollutants. Furthermore, reactive oxygen species trapping experiments allowed us to identify which active species play a significant role in the MO degradation process. The Na_2EDTA, *t*-BuOH, and BQ are usually utilized to scavenge photogenerated holes (h^+), hydroxyl radicals (•OH), and superoxide radicals ($\bullet O_2^-$), respectively. Generally speaking, the specific scavengers can react with reactive species faster than MO molecules, resulting in the reduced degradation rate of MO. It is clearly observed that the degradation rate of MO by TC2 has been significantly impeded in the presence of BQ, followed by Na_2EDTA in Fig. 6D. This result implies that $\bullet O_2^-$ acts as the main active species in the process of MO photodegradation.

The photocatalytic H_2 evolution performance of the as-prepared samples was measured under xenon lamp irradiation using TEOA as a sacrificial agent as shown in Figs. 7A and 7B. Pure TiO_2 nanotubes exhibit a low H_2 generation rate (1714 $\mu mol \cdot g^{-1} \cdot h^{-1}$), while with the increase of the amount of g-C_3N_4, the rate of H_2 evolution is significantly enhanced (2987 and 4122 $\mu mol \cdot g^{-1} \cdot h^{-1}$ for TC1 and TC2, respectively). The further increase of g-C_3N_4 leads to a reduction of H_2 generation

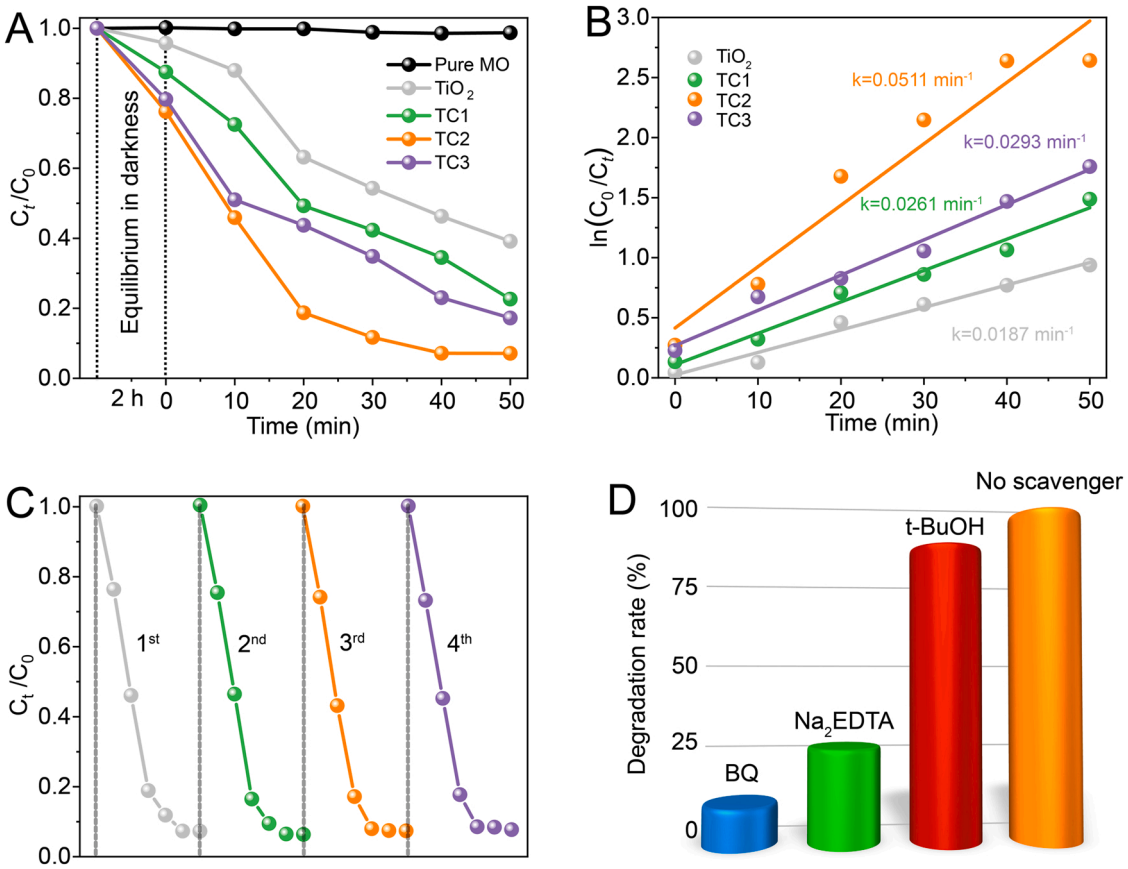

Fig. 6. The removal rates of MO by the photocatalysts under xenon lamp irradiation (A) and corresponding pseudo-first-order kinetics fitting data (B). The repeatability tests studied on the TC2 nanotubes for four cycles (C). The impact of various scavengers on MO photodegradation over TC2 (D).

(3120 μmol·g^{-1}·h^{-1} for TC3), which may be due to a decrease in active sites' exposure resulting from excessive g-C_3N_4 shielding. The TC2 exhibited the highest H_2 evolution rate, which is 2.4 times higher than pure TiO_2 nanotubes. Meanwhile, the photocatalytic stability of the TC2 was also investigated by four reaction cycles (2 h per cycle) under the same condition. As shown in Fig. 7C, no noticeable deactivation was observed in the long H_2 evolution, which means the high photocatalytic stability of the porous g-C_3N_4/TiO_2 composite nanotubes. In addition, the apparent quantum efficiency (AQE) of TC2 for photocatalytic H_2 evolution exhibits a notable quantum yield of 23.7% at $\lambda = 330$ nm (Fig. 7D), which approximately matches with the UV-Vis absorption spectrum.

3.3. Mechanism of photocatalytic performance enhancement

When the g-C_3N_4/TiO_2 composite nanotubes were excited by light, the efficiency of photo-induced electrons (e^-) and holes (h^+) is the key to the photocatalytic process. To determine the production of photo-generated e^- and h^+, the transient photocurrents of the TiO_2 and g-C_3N_4/TiO_2 (TC2) nanotubes were evaluated under xenon lamp irradiation. As shown in Fig. 8A, compared with the TiO_2 nanotubes, the g-C_3N_4/TiO_2 nanotubes show a stronger photo-generated current. And the magnitude of photocurrent changes little during on/off switching operation, demonstrating a stable photoelectrical performance of g-C_3N_4/TiO_2 nanotubes.

Photoluminescence (PL) spectra was measured to investigate the photo-induced charge transfer process of the composite nanotubes. As seen in Fig. 8B, the emission peak intensity of TC2 nanotubes is significantly lower than that of pure TiO_2 nanotubes. Since the recombination rate of photo-generated charge carriers is directly proportional to the PL peak intensity, the lower PL intensity of the TC2 nanotubes implies that the photo-generated charge carriers are seriously limited. [32] The EIS Nyquist plots of TiO_2 and TC2 nanotubes were also used to investigate the charge transfer resistance of the photo-induced carriers. As shown in Fig. 8C, the EIS radius of the TC2 nanotubes is smaller than that of bulk TiO_2 due to a lower electronic impedance and higher transfer efficiency in g-C_3N_4/TiO_2 nanotubes. [31].

The Mott-Schottky plots of pure TiO_2 nanotubes and bulk g-C_3N_4 present positive slopes, which indicate that the as-prepared samples possess an n-type semiconductor nature as shown in Figs. 8D and 8E. The flat-band potentials of the TiO_2 nanotubes and bulk g-C_3N_4 were estimated to be − 0.71 eV and − 1.12 eV (vs. Ag/AgCl), corresponding to − 0.51 eV and − 0.92 eV (vs. NHE), respectively. Since the flat-band potential of n-type semiconductors is close to the conduction band (CB) position. [36] Thus, the CB positions of TiO_2 nanotubes and pure g-C_3N_4 are about − 0.51 eV and − 0.92 eV (vs. NHE), respectively. Meanwhile, the valence band (VB) of TiO_2 nanotubes and pure g-C_3N_4 can be calculated to be 2.55 eV and 1.94 eV (vs. NHE) following the equation $E_{VB} = E_g + E_{CB}$.

Efficient charge separation is essential in improving the photocatalytic performance of g-C_3N_4/TiO_2 composite nanotubes. To further understand the relationship between g-C_3N_4 and TiO_2 on photocatalytic performance, the differential charge density of g-C_3N_4/TiO_2 heterostructure was calculated by first principles. The results are shown in Fig. 8F; the yellow and blue regions represent the net electron accumulation and depletion distributions. Obviously, h^+ are clustered in the g-C_3N_4 region, while e^- are clustered in the TiO_2 region, which is consistent with XPS results. In addition, the charge redistribution between g-C_3N_4 and TiO_2 mainly occurs at the interface region, meaning that the heterostructure is conducive to efficient charge transfer.

Based on the above experimental results and theoretical calculations, a possible charge transfer pathway of g-C_3N_4/TiO_2 in the photocatalytic

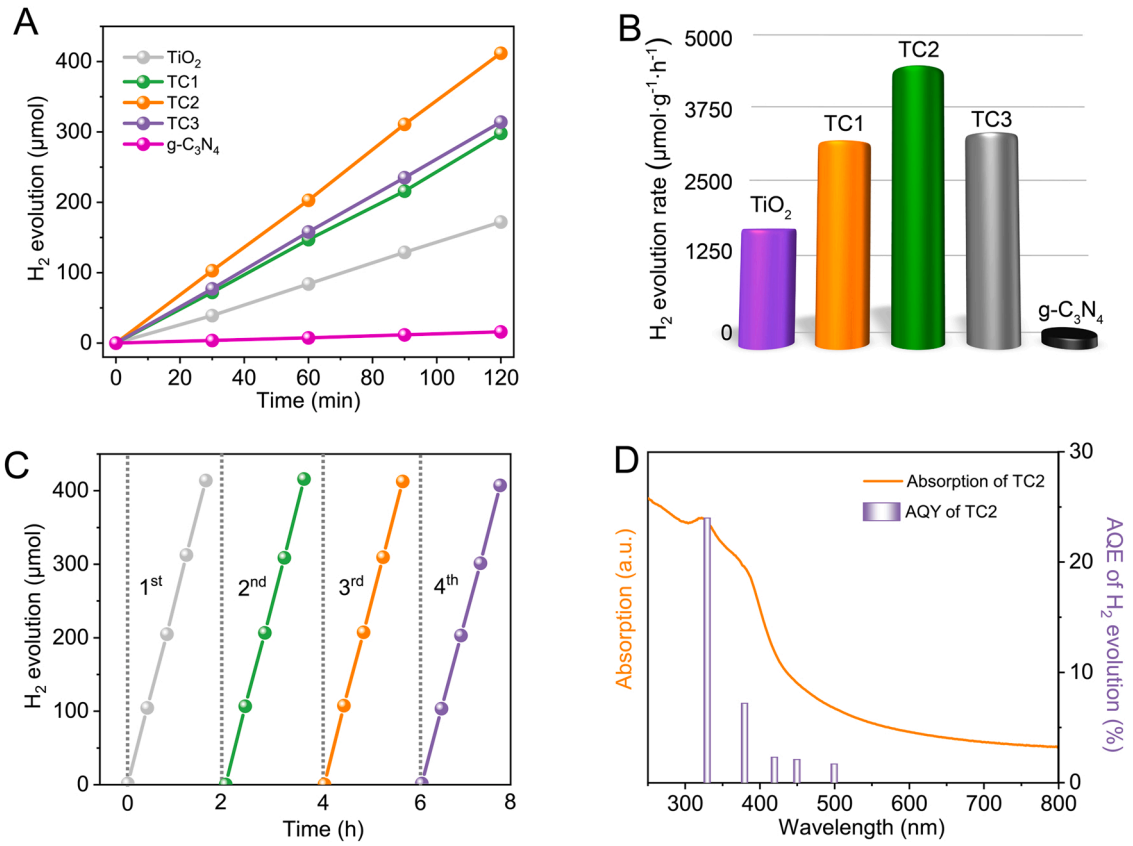

Fig. 7. The time-dependent H_2 evolution (A) and the rate of H_2 evolution (B) by the as-prepared photocatalysts under xenon lamp irradiation with the sacrificial agent of triethylamine. Stability study of photocatalytic H_2 evolution of TC2 nanotubes (C). Wavelength-dependent AQE for photocatalytic H_2 evolution (right axis) and UV-Vis light absorption spectrum (left axis) of TC2 nanotubes (D).

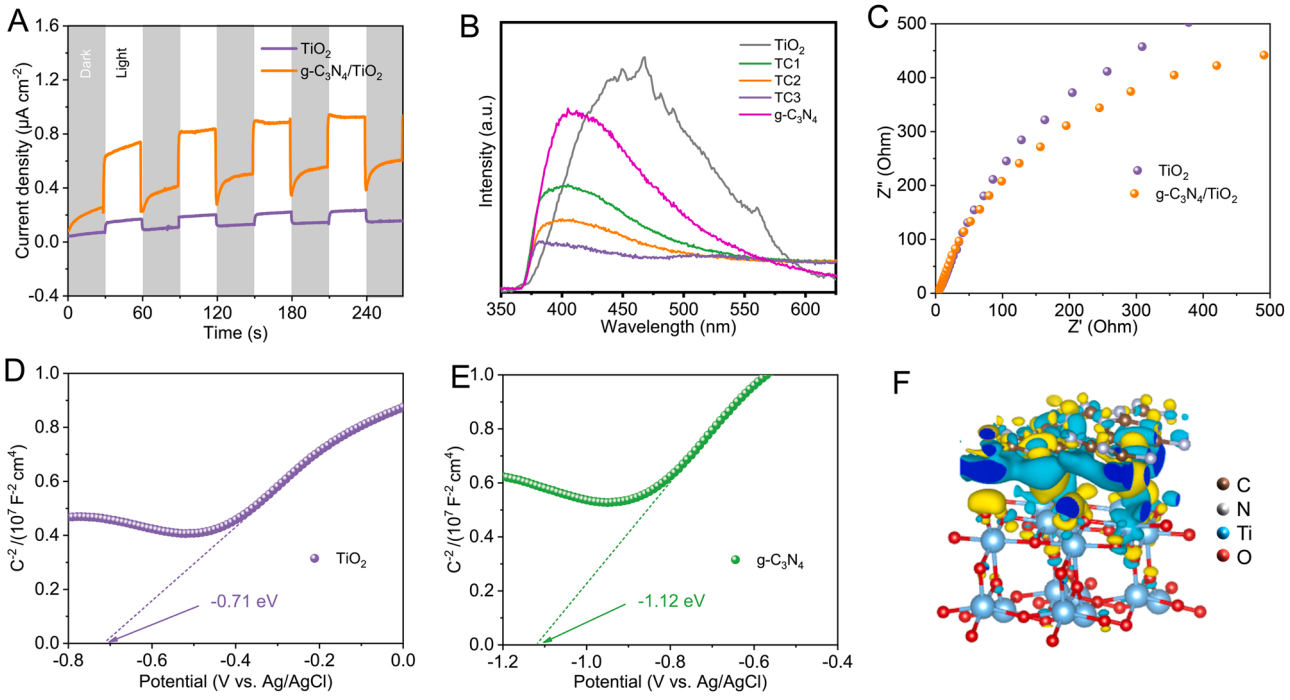

Fig. 8. The photocurrents spectra (A), the PL spectra (B), and the EIS Nyquist plots (C) of TiO_2 and g-C_3N_4/TiO_2 (TC2) nanotubes. The Mott-Schottky plots of TiO_2 nanotubes (D) and bulk g-C_3N_4 (E). The differential charge density of g-C_3N_4/TiO_2 heterojunction (F).

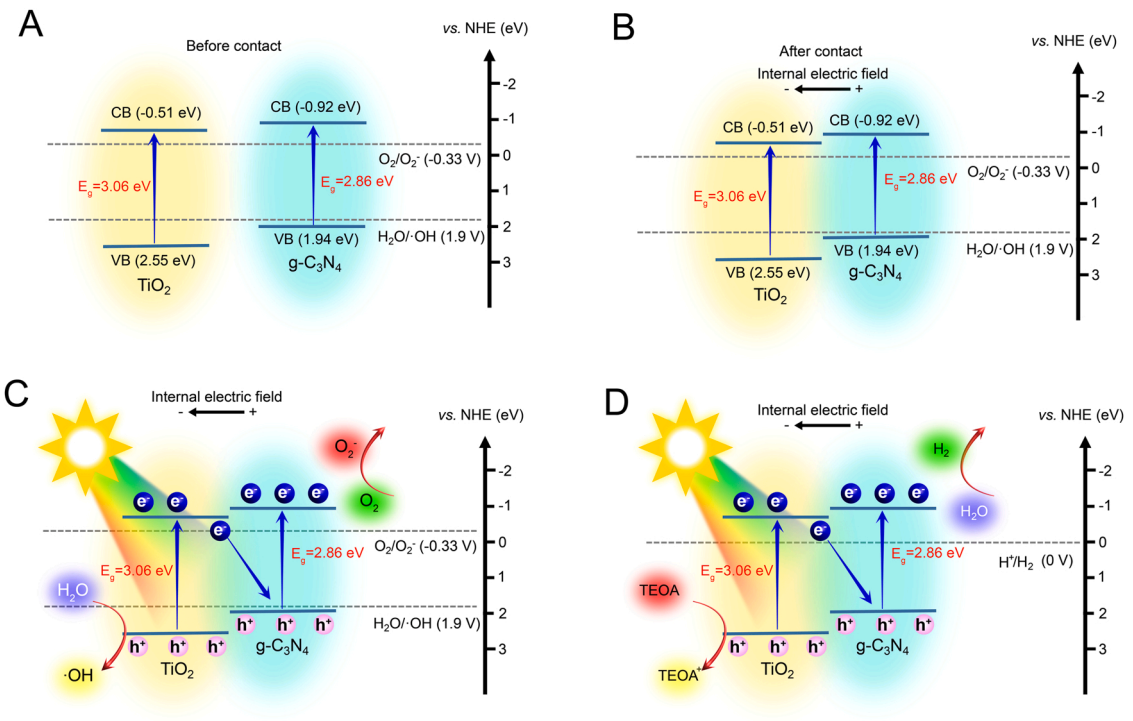

Fig. 9. Schematic illustration of the mechanism for the Z-scheme heterostructure in g-C_3N_4/TiO_2 nanotubes before contact (A) and after contact (B). Schematic of charge-transfer process of g-C_3N_4/TiO_2 nanotubes for photocatalytic degradation (C) and H_2 evolution (D) under xenon lamp irradiation.

process is delineated in Fig. 9. The band positions of each parts in g-C_3N_4/TiO_2 nanotubes can be evaluated by combining the analyses of UV-Vis DRS and Mott-Schottky plots as shown in Fig. 9A. The electrons in g-C_3N_4 can spontaneously transfer to TiO_2 nanotubes when the two semiconductors are in close proximity since the flat-band potential (conduction band position) of pure g-C_3N_4 is more negative than that of TiO_2 nanotubes. Consequently, the internal electric field forms on the interface of the two semiconductors directing from g-C_3N_4 to TiO_2 as shown in Fig. 9B, promoting the recombination of photo-generated h^+ in g-C_3N_4 and e^- in TiO_2 nanotubes in the photocatalytic process. [38] As a result, photo-generated e^- in g-C_3N_4 with stronger reduction ability and h^+ in TiO_2 with higher oxidation ability remained spatial separation, as shown in Fig. 9C, which implies a Z-scheme heterostructure charge transfer process in the g-C_3N_4/TiO_2 nanotubes. [39] Under xenon lamp irradiation, the photogenerated e^- can move from the VB to the CB of TiO_2 nanotubes and then transfer to g-C_3N_4 to recombine with h^+ under the action of the internal electric field. Thus, the h^+ in VB of TiO_2 and the e^- in CB of g-C_3N_4 are retained to participate in the reaction. The e^- in g-C_3N_4 can reduce the surface adsorbed oxygen to form $\bullet O_2^-$. The h^+ in TiO_2 mainly interact with the pollutant molecules directly, and some of them react with H_2O to generate $\bullet OH$. Eventually, organic pollutants are oxidized by these active species into CO_2 and H_2O as shown in Fig. 9C. The potential of g-C_3N_4 conduction band minimum is much negative than that of hydrogen evolution, which is enough for splitting the water molecule. Therefore, under the right environmental conditions (such as oxygen-free, sacrificial agent presence, etc), the accumulated electrons in g-C_3N_4 can directly react with H^+ ions to produce H_2 as shown in Fig. 9D.

4. Conclusions

In this study, porous g-C_3N_4/TiO_2 nanotubes were obtained via electrospinning combined with an ingenious vapor deposition method. The highly porous nanotube structure provided a large specific surface area, while the heterostructure enhanced the separation of photo-generated charge carriers. This g-C_3N_4/TiO_2 nanotube composite showed excellent photocatalytic activity for organic degradation and hydrogen production. Our work provides a facile avenue for fabricating heterostructures with porous nanotubes from waste resources and future applications in waste utilization and high-efficiency photocatalysis.

CRediT authorship contribution statement

Sheng-Zhe Zhao: Conceptualization, Investigation, Writing – original draft., **Ran Lu:** Supervision, Validation, Methodology, **Yi Yang:** Formal analysis, **Yun Lu:** Funding acquisition, **Raul D. Rodriguez:** Writing – review & editing, **Jin-Ju Chen:** Project administration, Funding acquisition.

Declaration of Competing Interest

The authors declare that they have no known competing financial interests or personal relationships that could have appeared to influence the work reported in this paper.

Data availability

The data that has been used is confidential.

Acknowledgements

The work was supported by the Sichuan Science and Technology Program (grant No 2023YFG0215), Russian Foundation for Basic Research (grant No 21-53-12045).

References

[1] X. Bao, H. Li, Z. Wang, F. Tong, M. Liu, Z. Zheng, P. Wang, H. Cheng, Y. Liu, Y. Dai, Y. Fan, Z. Li, B. Huang, TiO_2/Ti_3C_2 as an efficient photocatalyst for selective oxidation of benzyl alcohol to benzaldehyde, Appl. Catal. B: Environ. 286 (2021), 119885.
[2] Y. Fu, Z. Ren, J. Wu, Y. Li, W. Liu, P. Li, L. Xing, J. Ma, H. Wang, X. Xue, Direct Z-scheme heterojunction of ZnO/MoS_2 nanoarrays realized by flowing-induced

piezoelectric field for enhanced sunlight photocatalytic performances, Appl. Catal. B: Environ. 285 (2021), 119785.
[3] J. Cai, X. Wu, S. Li, F. Zheng, Controllable location of Au nanoparticles as cocatalyst onto TiO_2@CeO_2 nanocomposite hollow spheres for enhancing photocatalytic activity, Appl. Catal. B: Environ. 201 (2017) 12–21.
[4] X. Li, H. Jiang, C. Ma, Z. Zhu, X. Song, H. Wang, P. Huo, X. Li, Local surface plasma resonance effect enhanced Z-scheme ZnO/Au/g-C_3N_4 film photocatalyst for reduction of CO_2 to CO, Appl. Catal. B: Environ. 283 (2021), 119638.
[5] R. Zhong, Z. Zhang, S. Luo, Z.C. Zhang, L. Huang, M. Gu, Comparison of TiO_2 and g-C_3N_4 2D/2D nanocomposites from three synthesis protocols for visible-light induced hydrogen evolution, Catal. Sci. Technol. 9 (2019) 75–85.
[6] Z. Hou, J. Chu, C. Liu, J. Wang, A. Li, T. Lin, C.P. François-Xavier, High efficient photocatalytic reduction of nitrate to N_2 by Core-shell Ag/SiO_2@cTiO_2 with synergistic effect of light scattering and surface plasmon resonance, Chem. Eng. J. 415 (2021), 128863.
[7] X. Sun, W. He, X. Hao, H. Ji, W. Liu, Z. Cai, Surface modification of BiOBr/TiO_2 by reduced AgBr for solar-driven PAHs degradation: mechanism insight and application assessment, J. Hazard Mater. 412 (2021), 125221.
[8] Z. Cheng, S. Zhao, Z. Han, Y. Zhang, X. Zhao, L. Kang, A novel preparation of Ag@TiO_2 tubes and their potent photocatalytic degradation efficiency, CrystEngComm 18 (2016) 8756–8761.
[9] J. Liu, N. Ma, W. Wu, Q. He, Recent progress on photocatalytic heterostructures with full solar spectral responses, Chem. Eng. J. 393 (2020), 124719.
[10] Z. Cheng, S. Zhao, L. Han, A novel preparation method for ZnO/gamma-Al_2O_3 nanofibers with enhanced absorbability and improved photocatalytic water-treatment performance by Ag nanoparticles, Nanoscale 10 (2018) 6892–6899.
[11] S. Zhao, Z. Cheng, L. Kang, Y. Zhang, X. Zhao, A novel preparation of porous spong-shaped Ag/ZnO heterostructures and their potent photocatalytic degradation efficiency, Mater. Lett. 182 (2016) 305–308.
[12] S. Zhao, Z. Cheng, L. Kang, M. Li, Z. Gao, The facile preparation of Ag decorated TiO_2/ZnO nanotubes and their potent photocatalytic degradation efficiency, RSC Adv. 7 (2017) 50064–50071.
[13] Z. Dai, Y. Zhen, Y. Sun, L. Li, D. Ding, $ZnFe_2O_4$/g-C_3N_4 S-scheme photocatalyst with enhanced adsorption and photocatalytic activity for uranium(VI) removal, Chem. Eng. J. 415 (2021), 129002.
[14] M. Moradi, F. Hasanvandian, A.A. Isari, F. Hayati, B. Kakavandi, S.R. Setayesh, CuO and ZnO co-anchored on g-C_3N_4 nanosheets as an affordable double Z-scheme nanocomposite for photocatalytic decontamination of amoxicillin, Appl. Catal. B: Environ. 285 (2021), 119838.
[15] L. Matějová, K. Kočí, M. Reli, L. Čapek, A. Hospodková, P. Peikertová, Z. Matěj, L. Obalová, A. Wach, P. Kuśtrowski, A. Kotarba, Preparation, characterization and photocatalytic properties of cerium doped TiO_2: on the effect of Ce loading on the photocatalytic reduction of carbon dioxide, Appl. Catal. B: Environ. 152–153 (2014) 172–183.
[16] J. Wang, J. Ma, Q. Zhang, Y. Chen, L. Hong, B. Wang, J. Chen, H. Jing, New heterojunctions of CN/TiO_2 with different band structure as highly efficient catalysts for artificial photosynthesis, Appl. Catal. B: Environ. 285 (2021), 119781.
[17] H. Yan, R. Wang, R. Liu, T. Xu, J. Sun, L. Liu, J. Wang, Recyclable and reusable direct Z-scheme heterojunction CeO_2/TiO_2 nanotube arrays for photocatalytic water disinfection, Appl. Catal. B: Environ. 291 (2021), 120096.
[18] R. Guan, D. Wang, Y. Zhang, C. Liu, W. Xu, J. Wang, Z. Zhao, M. Feng, Q. Shang, Z. Sun, Enhanced photocatalytic N_2 fixation via defective and fluoride modified TiO_2 surface, Appl. Catal. B: Environ. 282 (2021), 119580.
[19] J. Fu, J. Yu, C. Jiang, B. Cheng, g-C_3N_4-based heterostructured photocatalysts, advanced energy, Materials 8 (2018) 1701503.
[20] G. Dong, P. Qiu, F. Meng, Y. Wang, B. He, Y. Yu, X. Liu, Z. Li, Facile synthesis of sulfur-doped polymeric carbon nitride/MoS_2 face-to-face heterojunction for highly efficient photocatalytic interfacial charge separation, Chem. Eng. J. 384 (2020), 123330.
[21] L. Luo, Z. Gong, J. Ma, K. Wang, H. Zhu, K. Li, L. Xiong, X. Guo, J. Tang, Ultrathin sulfur-doped holey carbon nitride nanosheets with superior photocatalytic hydrogen production from water, Appl. Catal. B: Environ. 284 (2021), 119742.
[22] L. Zhou, J. Lei, F. Wang, L. Wang, M.R. Hoffmann, Y. Liu, S.-I. In, J. Zhang, Carbon nitride nanotubes with in situ grafted hydroxyl groups for highly efficient spontaneous H_2O_2 production, Appl. Catal. B: Environ. 288 (2021), 119993.
[23] S. Wan, M. Ou, X. Wang, Y. Wang, Y. Zeng, J. Ding, S. Zhang, Q. Zhong, Facile fabrication of oxygen and carbon co-doped carbon nitride nanosheets for efficient visible light photocatalytic H_2 evolution and CO_2 reduction, Dalton Trans. 48 (2019) 12070–12079.
[24] H. Ming, D. Wei, Y. Yang, B. Chen, C. Yang, J. Zhang, Y. Hou, Photocatalytic activation of peroxymonosulfate by carbon quantum dots functionalized carbon nitride for efficient degradation of bisphenol A under visible-light irradiation, Chem. Eng. J. 424 (2021), 130296.
[25] T. An, J. Tang, Y. Zhang, Y. Quan, X. Gong, A.M. Al-Enizi, A.A. Elzatahry, L. Zhang, G. Zheng, Photoelectrochemical Conversion from Graphitic C_3N_4 Quantum Dot Decorated Semiconductor Nanowires, ACS Appl. Mater. Interfaces 8 (2016) 12772–12779.
[26] G. Liu, Y. Huang, H. Lv, H. Wang, Y. Zeng, M. Yuan, Q. Meng, C. Wang, Confining single-atom Pd on g-C_3N_4 with carbon vacancies towards enhanced photocatalytic NO conversion, Appl. Catal. B: Environ. 284 (2021), 119683.
[27] W. Zou, X.-H. Liu, C. Xue, X.-T. Zhou, H.-Y. Yu, P. Fan, H.-B. Ji, Enhancement of the visible-light absorption and charge mobility in a zinc porphyrin polymer/g-C_3N_4 heterojunction for promoting the oxidative coupling of amines, Appl. Catal. B: Environ. 285 (2021), 119863.
[28] X. Zhou, C. Shao, X. Li, X. Wang, X. Guo, Y. Liu, Three dimensional hierarchical heterostructures of g-C_3N_4 nanosheets/TiO_2 nanofibers: Controllable growth via gas-solid reaction and enhanced photocatalytic activity under visible light, J. Hazard Mater. 344 (2018) 113–122.
[29] X. Hu, P. Lu, R. Pan, Y. Li, J. Bai, Y. He, C. Zhang, F. Jia, M. Fu, Metal-ion-assisted construction of cyano group defects in g-C_3N_4 to simultaneously degrade wastewater and produce hydrogen, Chem. Eng. J. 423 (2021), 130278.
[30] G. Li, Z. Xie, S. Chai, X. Chen, X. Wang, A facile one-step fabrication of holey carbon nitride nanosheets for visible-light-driven hydrogen evolution, Appl. Catal. B: Environ. 283 (2021), 119637.
[31] Y. Sheng, Z. Wei, H. Miao, W. Yao, H. Li, Y. Zhu, Enhanced organic pollutant photodegradation via adsorption/photocatalysis synergy using a 3D g-C_3N_4/TiO_2 free-separation photocatalyst, Chem. Eng. J. 370 (2019) 287–294.
[32] R. Hao, G. Wang, H. Tang, L. Sun, C. Xu, D. Han, Template-free preparation of macro/mesoporous g-C_3N_4/TiO_2 heterojunction photocatalysts with enhanced visible light photocatalytic activity, Appl. Catal. B: Environ. 187 (2016) 47–58.
[33] X. Yang, Y. Zhang, Y. Wang, C. Xin, P. Zhang, D. Liu, B.B. Mamba, K.K. Kefeni, A. T. Kuvarega, J. Gui, Hollow β-Bi_2O_3@CeO_2 heterostructure microsphere with controllable crystal phase for efficient photocatalysis, Chem. Eng. J. 387 (2020), 124100.
[34] Q. Chen, W. Yang, J. Zhu, L. Fu, D. Li, L. Zhou, Enhanced visible light photocatalytic activity of g-C_3N_4 decorated ZrO_{2-x} nanotubes heterostructure for degradation of tetracycline hydrochloride, J. Hazard Mater. 384 (2020), 121275.
[35] H.S. Moon, K.C. Hsiao, M.C. Wu, Y. Yun, Y.J. Hsu, K. Yong, Spatial separation of cocatalysts on Z-scheme organic/inorganic heterostructure hollow spheres for enhanced photocatalytic h_2 evolution and in-depth analysis of the charge-transfer mechanism, Adv. Mater. (2022), e2200172.
[36] J. Ran, W. Guo, H. Wang, B. Zhu, J. Yu, S.Z. Qiao, Metal-free 2D/2D phosphorene/g-C_3N_4 van der waals heterojunction for highly enhanced visible-light photocatalytic H_2 production, Adv. Mater. 30 (2018), e1800128.
[37] S. Ma, W. Song, B. Liu, W. Zhong, J. Deng, H. Zheng, J. Liu, X.-Q. Gong, Z. Zhao, Facet-dependent photocatalytic performance of TiO_2: A DFT study, Appl. Catal. B: Environ. 198 (2016) 1–8.
[38] C. Xu, D. Li, X. Liu, R. Ma, N. Sakai, Y. Yang, S. Lin, J. Yang, H. Pan, J. Huang, T. Sasaki, Direct Z-scheme construction of g-C_3N_4 quantum dots/TiO_2 nanoflakes for efficient photocatalysis, Chem. Eng. J. 430 (2022), 132861.
[39] X. Ma, Q. Chen, G. Liu, Y. Zhou, D. Ma, S. Xin, C. Yu, B. Zhang, Y. Xin, Construction of netlike 3D Z-scheme photoelectrodes with improved photocatalytic performance based on g-C_3N_4 nanosheets modified TiO_2 nanobelt-tubes, Chem. Eng. Sci. 226 (2020), 115844.